



HAL
open science

Seismic observation of an extremely magmatic accretion at the ultraslow spreading Southwest Indian Ridge

Jiabiao Li, Hanchao Jian, Yongshun John Chen, Satish C. Singh, Aiguo Ruan,
Xuelin Qiu, Minghui Zhao, Xianguang Wang, Xiongwei Niu, Jianyu Ni, et al.

► **To cite this version:**

Jiabiao Li, Hanchao Jian, Yongshun John Chen, Satish C. Singh, Aiguo Ruan, et al.. Seismic observation of an extremely magmatic accretion at the ultraslow spreading Southwest Indian Ridge. *Geophysical Research Letters*, 2015, 42, pp.2656-2663. 10.1002/2014GL062521 . insu-03579979

HAL Id: insu-03579979

<https://insu.hal.science/insu-03579979>

Submitted on 18 Feb 2022

HAL is a multi-disciplinary open access archive for the deposit and dissemination of scientific research documents, whether they are published or not. The documents may come from teaching and research institutions in France or abroad, or from public or private research centers.

L'archive ouverte pluridisciplinaire **HAL**, est destinée au dépôt et à la diffusion de documents scientifiques de niveau recherche, publiés ou non, émanant des établissements d'enseignement et de recherche français ou étrangers, des laboratoires publics ou privés.

Copyright



RESEARCH LETTER

10.1002/2014GL062521

Key Points:

- We observe an extremely thick crust (~9.5 km) at an ultraslow spreading segment
- A low-velocity anomaly within the thick crust suggests the presence of melt
- A significant crustal thickness variation indicates a highly focused melt supply

Supporting Information:

- Figures S1–S6

Correspondence to:

Y. J. Chen,
johnyc@pku.edu.cn

Citation:

Li, J., et al. (2015), Seismic observation of an extremely magmatic accretion at the ultraslow spreading Southwest Indian Ridge, *Geophys. Res. Lett.*, 42, 2656–2663, doi:10.1002/2014GL062521.

Received 17 NOV 2014

Accepted 3 FEB 2015

Accepted article online 6 FEB 2015

Published online 19 APR 2015

Seismic observation of an extremely magmatic accretion at the ultraslow spreading Southwest Indian Ridge

Jiabiao Li¹, Hanchao Jian^{2,3}, Yongshun John Chen², Satish C. Singh³, Aiguo Ruan¹, Xuelin Qiu⁴, Minghui Zhao⁴, Xianguang Wang², Xiongwei Niu¹, Jianyu Ni¹, and Jiazheng Zhang⁴

¹Second Institute of Oceanography, State Oceanic Administration, Hangzhou, China, ²Institute of Theoretical and Applied Geophysics, School of Earth and Space Science, Peking University, Beijing, China, ³Laboratoire de Géosciences Marines, Institut de Physique du Globe de Paris, Paris, France, ⁴South China Sea Institute of Oceanology, Chinese Academy of Sciences, Guangzhou, China

Abstract The oceanic crust is formed by a combination of magmatic and tectonic processes at mid-ocean spreading centers. Under ultraslow spreading environment, however, observations of thin crust and mantle-derived peridotites on the seafloor suggest that a large portion of crust is formed mainly by tectonic processes, with little or absence of magmatism. Using three-dimensional seismic tomography at an ultraslow spreading Southwest Indian Ridge segment containing a central volcano at 50°28'E, here we report the presence of an extremely magmatic accretion of the oceanic crust. Our results reveal a low-velocity anomaly (−0.6 km/s) in the lower crust beneath the central volcano, suggesting the presence of partial melt, which is accompanied by an unusually thick crust (~9.5 km). We also observe a strong along-axis variation in crustal thickness from 9.5 to 4 km within 30–50 km distance, requiring a highly focused melt delivery from the mantle. We conclude that the extremely magmatic accretion is due to localized melt flow toward the central volcano, which was enhanced by the significant along-axis variation in lithosphere thickness at the ultraslow spreading Southwest Indian Ridge.

1. Introduction

Ultraslow spreading ridges are extreme end-members of mid-ocean ridges with full-spreading rates less than 20 mm/yr [Dick *et al.*, 2003]. They are highly variable in terms of melt supply, which has influences on the axial depth, the obliquity of spreading and the presence or absence of long-lived transform and nontransform discontinuities (NTD) [Cannat *et al.*, 2008; Dick *et al.*, 2003; Michael *et al.*, 2003]. The Southwest Indian Ridge (SWIR), despite spreading at an almost constant full rate of ~14 mm/yr between the Prince Edward Fracture Zone (FZ, Figure 1a) and its eastern end at 70°E [DeMets *et al.*, 1994; Horner-Johnson *et al.*, 2005], has all these characteristics. For example, the regional mean water depth changes from >4300 m in the east to <3500 m in the west [Cannat *et al.*, 2008] across the Gallieni FZ (Figure 1a), reflecting a large-scale variation in melt supply. Although based on the presence of thin crust [Cannat *et al.*, 2006; Jokat and Schmidt-Aursch, 2007; Minshull *et al.*, 2006] and mantle-derived peridotites on the seafloor [Dick *et al.*, 2003; Michael *et al.*, 2003; Zhou and Dick, 2013], tectonic extension dominating crustal accretion on ultraslow spreading ridges has been extensively documented, requiring little melt supply, regions with shallow bathymetry would require enhanced melt supply.

Here we study a shallow segment on the SWIR at 50°28'E with active-source seismic experiments. The segment lies between the Gallieni FZ and Indomed FZ, where the ridge axis has an overall obliquity of 25° [Cannat *et al.*, 2008] and is devoid of any long-lived discontinuities (Figure 1a). This region of the ridge axis has a mean axial depth of ~3180 m [Sauter *et al.*, 2009] (compared to a mean axial depth greater than 4000 m at other segments of SWIR) and distinct volcanic centers, suggesting a robust melt supply. We studied a ~60 km long segment (segment 27 [Cannat *et al.*, 1999]) that contains a central volcano rising up to 1390 m water depth (Figures 1b and S1 in the supporting information), one of the shallowest volcanoes along the SWIR. The low mantle Bouguer gravity anomaly (MBA, −84 mGal) [Sauter *et al.*, 2009] suggests the presence of a thick crust or low-density materials in the crust or in the upper mantle. An extinct hydrothermal vent field was recently discovered near the central volcano [Tao *et al.*, 2012]. The main bounding faults are separated by a 20–25 km wide median valley [Mendel *et al.*, 2003], similar to the Lucky Strike segment at the

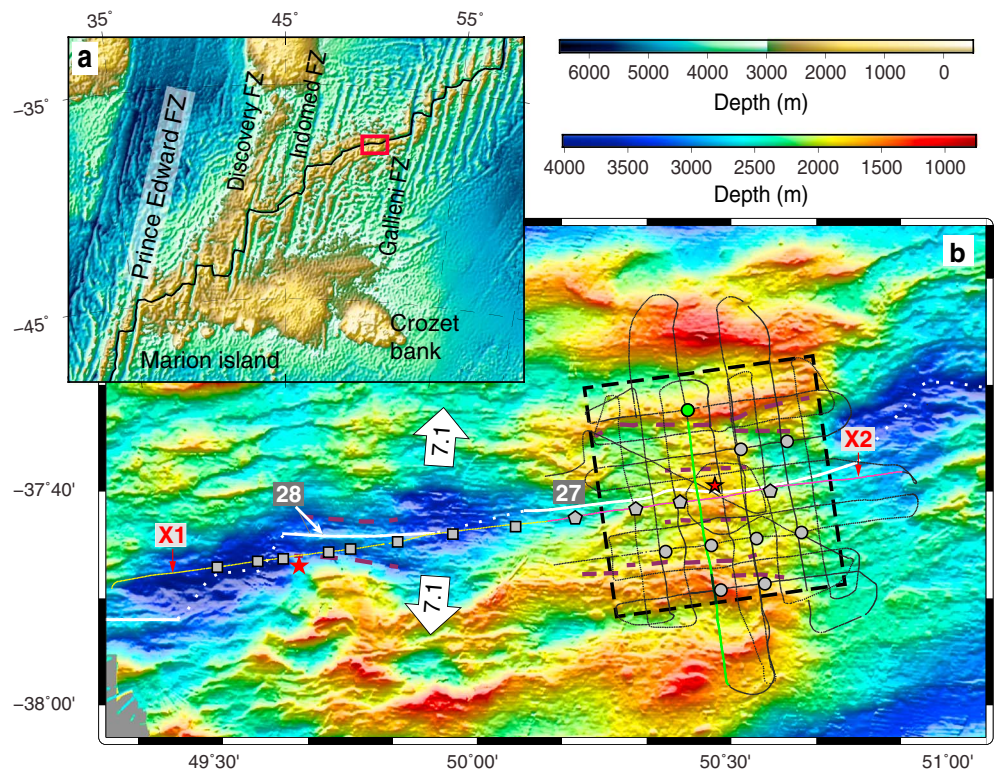


Figure 1. Study area. (a) Bathymetric map of the Southwest Indian Ridge (black curve), fracture zones (FZ), and off-axis high-topography edifices. Red rectangle marks the area shown in Figure 1b. (b) Bathymetric map of the seismic survey area. Dotted curves indicate the track of shots used only in the 3-D tomography (black and green), only in the 2-D tomography (yellow), and in both (magenta). The symbols represent ocean bottom seismometers (OBS), circles for those used only in 3-D tomography, squares when only used in 2-D tomography, and pentagons when used in both. Ridge axis of segments 27 and 28 are shown as solid white lines and nontransform discontinuities (NTD) as dashed white lines. The dark red dashed curves are the bounding faults. The red star is an active hydrothermal vent and the black-edged one represents an extinct vent. The spreading direction and half rate (NUVEL-1A) [DeMets *et al.*, 1994] are given in mm/yr on white arrows. The green color marks the OBS and shots shown in Figure 2. The black dashed line indicates the location of slices shown in Figures 3e and 3f. X1 and X2 are the end points of the along-axis profile shown in Figures 4 and S6.

slow spreading Mid-Atlantic Ridge (MAR) [Singh *et al.*, 2006], indicating magmatic-tectonic processes. A small narrow segment (segment 28) lies farther west and has a narrow neovolcanic ridge at its center, bounded by a steeply dipping fault in the south where an active high-temperature hydrothermal vent was discovered [Tao *et al.*, 2012]. A small NTD separating the two segments is recognized as a deep basin.

2. Seismic Experiment and Tomographic Inversions

We acquired three-dimensional (3-D) seismic refraction data using ocean bottom seismometers (OBS) in February 2010 on board the Chinese R/V *Dayang Yihao*. A total of 40 OBS were deployed, of which we used two subsets in this study (Figure 1b): (1) a 3-D box consisting of 13 OBS covering the central volcano of segment 27 and (2) a 2-D profile consisting of 12 OBS connecting the two segments (27 and 28) of the ridge axis. Results of a second 3-D array of 18 OBS centered at the western end of segment 28 were reported in a separate study [Zhao *et al.*, 2013]. We used an array of four air guns as a source, and each air gun has a volume of 1500 in³ (~24.6 L). Shots were fired every 2 min (~240 m) along a grid of lines spaced at ~4 km for the 3-D study and along a 135 km long profile for the 2-D study.

Figure 2a shows an example of the OBS data along a N-S profile running across the axis at the segment center (Figure 1b), where the crustal refraction (Pg) can be observed up to 27 km offset. After that, the amplitude of the Pg arrival is much reduced, creating a shadow zone, which is followed by a strong wide-angle reflection from the Moho (PmP) that can be observed up to 48 km offset. The good quality of the data (Figures 2a and S2) allows the accurate picking of both Pg and PmP arrivals and thus estimations of *P* wave velocity down to the

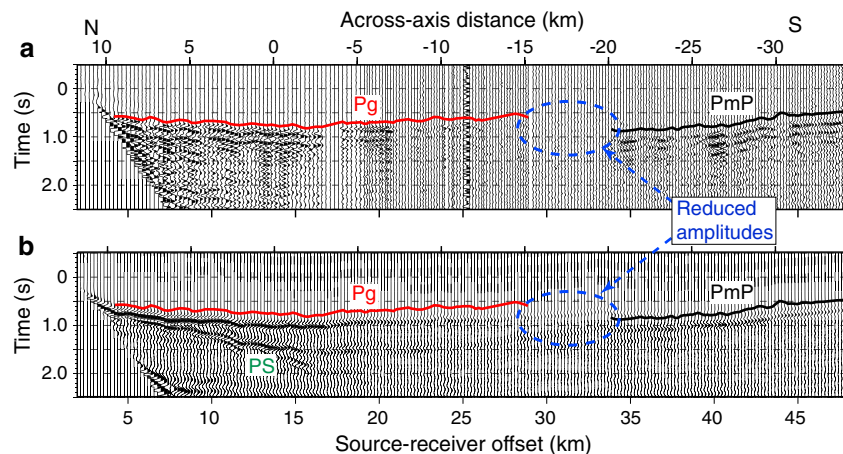


Figure 2. Seismic data. (a) Seismic record from one OBS and (b) synthetic seismogram generated from the inversion results shown in Figure 3. The locations of OBS and shots are shown in Figure 1b. The thick curves indicate the manually picked arrivals for Pg and PmP with red and black colors, respectively. PS indicates the P to S converted phase. A Ricker wavelet with a dominant frequency of 5 Hz is used as source in the modeling. A reduction velocity of 6.5 km/s and a water path correction are applied. A band-pass filter is applied for display purpose. The observed and synthetic waveforms are scaled to take spherical and cylindrical spreading effects into account, respectively. The ellipses indicate the shadow zone, which can be predicted by the best fitting model with a low-velocity anomaly in the lower crust.

Moho depth. In the 3-D box, we manually picked 50,228 Pg and 4563 PmP arrivals, with root-mean-square (RMS) of picking uncertainties as 32 ms and 46 ms, respectively. Both arrivals were inverted simultaneously for the 3-D velocity and Moho depth structure. Along the 2-D profile, we had 2586 first-arrival picks, with an RMS of picking uncertainties of 32 ms, and correspondingly, only the velocity structure was updated.

We adopted the iterative tomography method developed by *Van Avendonk et al.* [1998] and *Van Avendonk et al.* [2004] to seek best fitting velocity models in the 3-D box and along the 2-D profile, respectively. A 1-D starting model similar to crustal seismic models at the slow spreading MAR [*Seher et al.*, 2010] was hung from the seafloor, due to the similarity in the bathymetric and gravimetric observations. In the 3-D tomography, a Moho reflector at 10.5 km depth below the sea level was also added to the starting model. The traveltime residual normalized by the picking uncertainty had an initial RMS of 4 that reduced to 1 after the inversion (Figure S3). Checkerboard tests for the 3-D tomography show good resolution in the central 20 km by 20 km area, and an example is present in Figure S4.

Along the 2-D profile, because of relatively sparse ray coverage, practically of PmP reflections, we only inverted for a smooth crustal velocity model without a Moho interface to reduce the number of model parameters. The ray tracing was calculated in 3-D to account for the off-line effect, whereas the inversion is in 2-D as the model updates were averaged in the cross-line direction. Checkerboard tests for the 2-D tomography indicate good resolution along the profile, except in the lower crust beneath the center of segment 27 where the ray density is relatively low within the 2-D subset (Figure S4). However, this part of the crust is well resolved by the 3-D tomography, and the 2-D tomography was guided in this region by applying a strong damping toward the best fitting 3-D model during the inversion, which also ensures the consistency between the two inversions. The final normalized residual was close to 1, i.e., the data were fit to a RMS value of ~ 32 ms (Figure S3). Finally, the Moho structure near the center of segment 27 was constrained using the 3-D tomography model. The rest was estimated based on the absolute velocity and the vertical velocity gradient where we can observe a mantle velocity greater than 7.3 km/s, or from interpolation, as shown in Figures 4 and S6.

3. Results and Interpretation

Cross sections from the best fitting model in the 3-D box are shown in Figure 3. Both the across-axis and along-axis cross sections of the 3-D model of velocities (Figures 3a and 3c) and of anomalies (Figures 3b and 3d) show a clear evidence of a low-velocity anomaly (LVA) in the lower crust beneath the central volcano. From this best fitting model, we computed synthetic seismograms (Figure 2b) using a 2-D finite-difference modeling

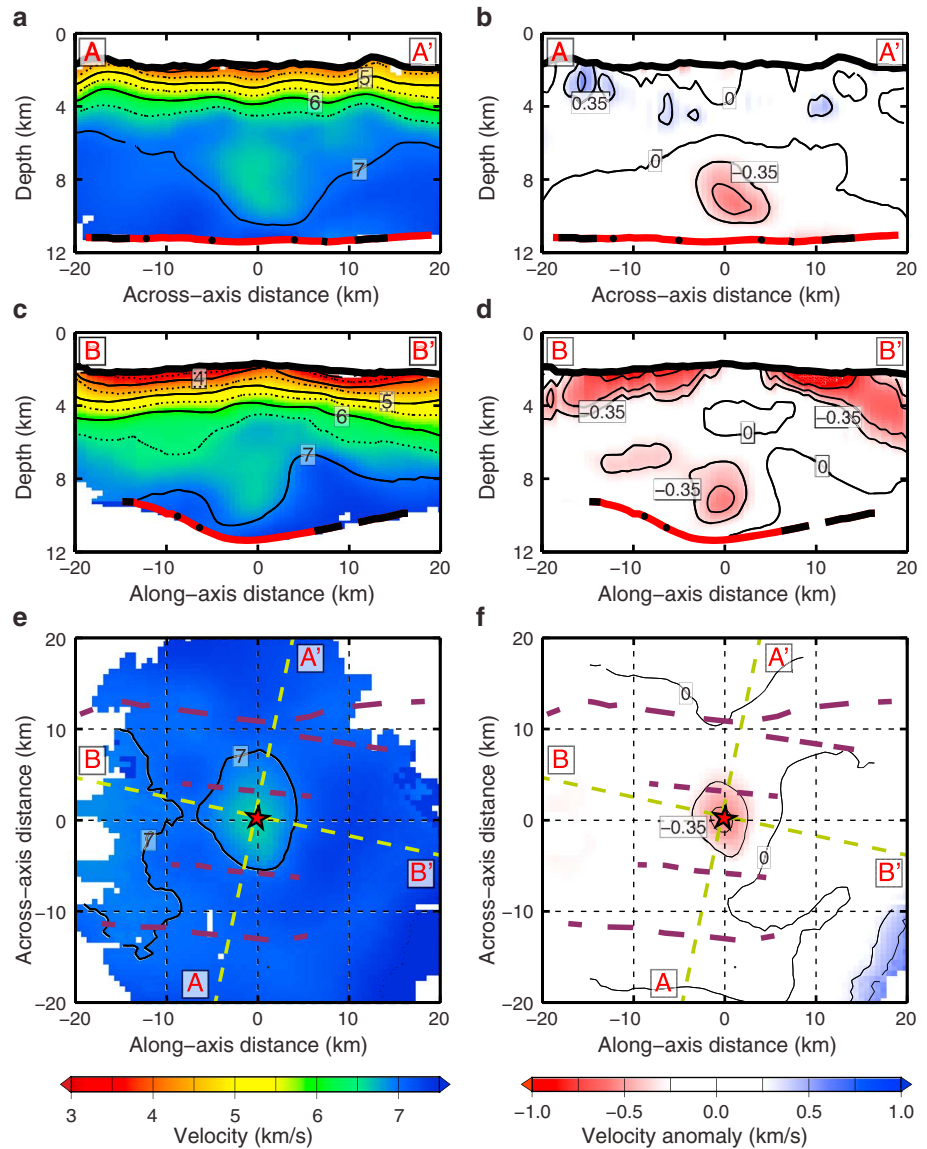


Figure 3. Three-dimensional velocity model result. Cross sections of velocity models ((a) across-axis and (c) along-axis) and anomalies ((b) across-axis and (d) along-axis) from the 3-D tomographic results, whose horizontal locations are marked in Figures 3e and 3f as dashed lines AA' and BB', respectively. These sections run parallel and perpendicular to the spreading direction. Lower boundaries correspond to Moho interface. The red color marks the reflecting points. The vertical exaggeration is 2:1. (e) Horizontal velocity and (f) anomaly slice of the 3-D velocity model at 7 km depth beneath the seafloor, whose location is marked in Figure 1b. The dark red dashed curves and the black-edged red star mark the bounding faults and the extinct vent. The contours (thin black curves) of velocities have an interval of 0.5 km/s, and the contour levels of anomalies are 0, ± 0.35 and ± 0.5 km/s. The anomaly model is calculated by subtracting from the 3-D model its 1-D average. The amplitude of the lower crustal low-velocity anomaly is >0.6 km/s. The crust is ~ 9.5 km thick at the center.

method [Shipp and Singh, 2002]. The synthetic seismograms are good matches to the observed traveltimes as well as to the amplitudes, particularly of the shadow zone (Figure 2), indicating that the LVA is linked to the observed shadow zone. The LVA is round shaped with a diameter of 5–8 km, starts at 4–5 km below the seafloor, and extends down to 8–9 km depth (Figure 3), close to the Moho. The maximum anomaly of 0.6 km/s is centered at 7 km below the seafloor (Figures 3). Although part of the anomaly could be ascribed to a high temperature, a 0.6 km/s anomaly would require the presence of a small amount of melt in the lower crust [Dunn et al., 2000, 2005; Seher et al., 2010]. Since the tomography provides only a smooth model and tends to

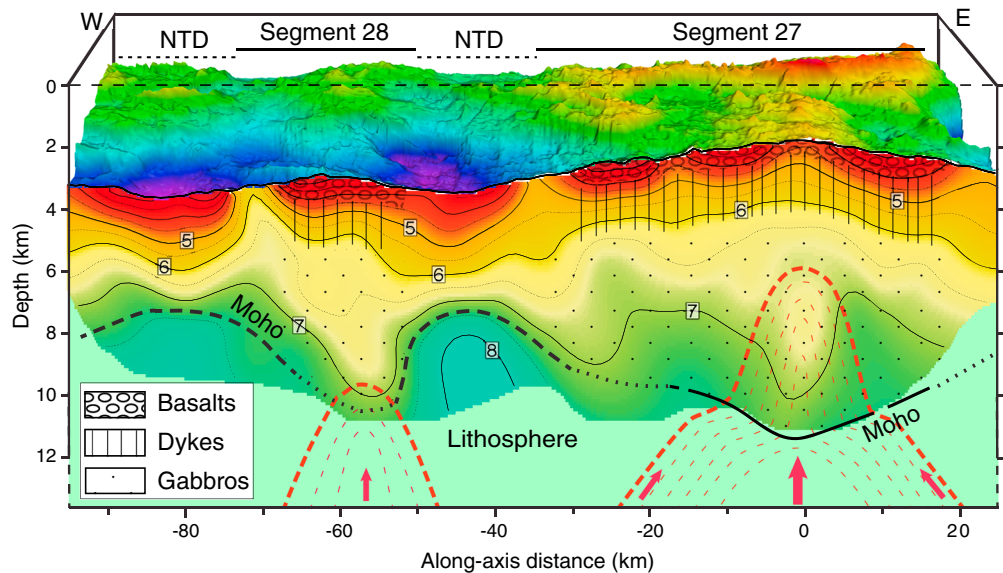


Figure 4. Two-segment along-axis velocity. A 3-D block diagram showing bathymetry and 2-D along-axis interpreted velocity. The thickness of basalt is only indicative because of the poor constraint on very shallow structure (hundreds of meters) of OBS data set. Thick black curves represent the position of the Moho extracted from the 3-D tomography model (solid), inferred from underlying mantle velocities (> 7.3 km/s) (dashed) and from interpolation (dotted). The velocity contours are marked as black thin curves, and numbers indicate velocity in km/s. The thin red dashed curves indicate the interpreted isotherms, and the thick ones indicate the solidus. The arrows at the bottom indicate the focused melt delivery. The vertical exaggeration is 4:1.

underestimate the low-velocity anomalies, it is difficult to quantify the amount of melt, but to reduce the velocity by 0.6 km/s in such deep crust, one could expect $\sim 10\%$ of partial melt [Taylor and Singh, 2002].

Our results also show that the crust is as thick as ~ 9.5 km beneath the central volcano and remains thick across the axis (Figure 3a). This is among the thickest oceanic crusts at global mid-ocean ridges without obvious influences of on-axis or near-axis plumes (Figure S5). The thick crust formed around the central volcano is composed of a high vertical velocity gradient layer and an underlying low vertical gradient layer (Figure 3a), which are typical layer 2 (dykes and pillow lava) and layer 3 (gabbro) for the igneous oceanic crust, indicating the magmatic accretion [Canales et al., 2000]. Interestingly, the round-shaped lower crustal LVA is located directly within the thickest crust (Figure 3d), suggesting an intimate link between the localized LVA and the thickened crust as a consequence of enhanced melt supply from the upper mantle beneath.

The along-axis variation of the crustal structure is further illuminated by the 2-D tomography results connecting the two segments (27 and 28), which are separated by a small NTD (Figures 4 and S6). The crustal thickness decreases from ~ 9.5 km at the center of segment 27 to ~ 4 km beneath the NTD and then again increases to ~ 7 km at segment 28, consistent with the other 3-D tomography result [Zhao et al., 2013]. Assuming that a velocity of 6.3 km/s marks the boundary between layer 2 and layer 3, the along-axis profiles (Figures 3c and 4) show a constant thickness of layer 2 (~ 3 km) near segment centers with a thick layer 3 underneath. However, beneath the NTD, the 6.3 km/s contour extends deeper with a smoother velocity gradient and a very thin gabbroic velocity underneath, similar to seismic models at relatively magma poor segments of ultraslow spreading ridges [Jokat et al., 2012; Minshull et al., 2006]. Together with the thin crust there, it indicates much less melt supply to the NTD and/or a thicker lithosphere underneath.

4. Discussion and Conclusion

Dick et al. [2003] have proposed the coexistence of linked magmatic and amagmatic extensions at ultraslow spreading ridges. While the amagmatic extension characterizing this novel class of spreading centers has been extensively observed with vast expanses of mantle-derived peridotites and highly tectonized seafloor [Cannat et al., 2006; Sauter et al., 2013; Zhou and Dick, 2013], the magmatic extension seems to be limited to a

widely spaced set of narrow magmatic centers. Indeed, our results indicate that the magmatism is a dominant process at the magmatic center, but the super thick crust and excess melt supply are less expected.

Furthermore, the significant crustal thickness variation along the ridge axis requires a highly localized melt delivery from the upper mantle, which has been proposed from other observations at slow and ultraslow spreading ridges [Cannat *et al.*, 2003; Hooft *et al.*, 2000; Sauter *et al.*, 2004; Schlindwein *et al.*, 2013; Standish *et al.*, 2008; Tolstoy *et al.*, 1993]. At slow/ultraslow spreading ridges or in cold regions, where the degree of melting is low, these small amounts of melt may migrate upward along a steeply dipping permeability barrier at the base of the lithosphere [Cannat *et al.*, 2003; Montesi *et al.*, 2011; Standish *et al.*, 2008] by a 3-D buoyancy-driven flow to isolated volcanic centers [Magde and Sparks, 1997; Montesi *et al.*, 2011]. For this to happen at segment 27, the lithosphere must be thick at the segment ends and beneath the NTDs (common at ultraslow ridges) and thin beneath the segment center (Figure 4), leading to a slope in the lithosphere-asthenosphere boundary (LAB) along which the melt can migrate and accumulate in the lower crust at the segment center and feed a ~60 km segment. Although we do not observe any melt beneath segment 28, its presence cannot be easily excluded within a 7 km thick crust, as our 2-D tomography is incapable of imaging a small LVA. However, at the narrow segment 28 the melt supply should be much less and the underneath mantle should be colder comparing to segment 27 (Figure 4). Consequently, a large-scale slope of the LAB may exist.

While a thicker crust at the center of segment 27 was suggested from the gravity data [Sauter *et al.*, 2009] as compared to the global average oceanic crustal thickness (6 km) [Chen, 1992], our seismic observation reveals an extremely thick crust, up to ~9.5 km. More importantly, this extremely thick crust can be traced to ~20 km off axis along the spreading direction (Figure 3a), indicating that this enhanced melt supply event has been persistent for at least the past 3 Ma. The elevated bathymetry farther off axis suggests that this melt anomaly could have been existing for up to 10 Ma [Sauter *et al.*, 2009]. The average crustal thickness within segment 27 is slightly more than 6 km, which is close to the global average at faster spreading ridges, but far more than the previously reported crustal production at ultraslow spreading ridges [e.g., Jokat and Schmidt-Aursch, 2007; Minshull *et al.*, 2006].

This extreme magmatism could be due to a hot mantle originated at the off-axis Crozet hot spot [Sauter *et al.*, 2009] 1000 km to the south. However, there are no bathymetric features supporting such a long-distance plume-ridge interaction. Although a contamination of the mantle below the SWIR between the Gallieni and Indomed FZ by Crozet plume material has been recently suggested based on the high ^3He signature [Breton *et al.*, 2013], other isotopic observations barely require this plume-ridge interaction [Meyzen *et al.*, 2005]. A recent global study also shows that the mantle potential temperature below our study area is only ~1380°C, less than the median value of 1395°C for global mid-ocean ridges [Dalton *et al.*, 2014], suggesting no significant influence of plumes. More essentially, the mechanism of such an interaction through a >1000 km conduit from an off-axis hot spot is challenging. Thus, we exclude that the influence from the Crozet hot spot could cause such extreme magmatism observed here.

Alternatively, the anomaly of the melt supply could be linked to heterogeneity of the upper mantle source. Isotopic analysis shows large heterogeneity along the SWIR to the west of the Indomed FZ (Figure 1a), where the presence of recycled continental lower crust is required [Mahoney *et al.*, 1992; Meyzen *et al.*, 2005], but to the east, the isotopic compositions are much more homogeneous and do not require the presence of such continental materials [Meyzen *et al.*, 2005]. Zhou and Dick [2013] have recently suggested that the high geoid of Marion Rise (including our study area) is supported by a buoyant depleted mantle, which is related to mantle plumes in the early history of the Earth. However, to produce a large amount of melt, a fertile mantle with continental crustal fragments or subducted sediments is required, for which there is no evidence from the isotopic data to date.

So far, there is no clear evidence of any influence from either hot spots or relicts from early history that could produce the extremely thick crust. Hence, we conclude that the combination of moderate mantle heterogeneity (a higher temperature or a fertile source) and a very efficient focusing mechanism of melt delivery is the cause of the extremely magmatic accretion. A similar coupling of a strong focusing effect and thick crust has been predicted by numerical models under the ultraslow spreading environment, which also predicted the replacement of transform faults by amagmatic segments to separate the magmatic segments [Puthe and Gerya, 2014]. It is possible that the large magmatic center with a thin lithosphere like segment 27 can collect melt in the asthenosphere from a wide surrounding area overlain by a very thick lithosphere,

which is common for ultraslow spreading ridges. The collecting area should be enlarged as these large magmatic centers are widely spaced and the transform or large nontransform offsets acting as effective thermal boundaries are systematically absent at ultraslow spreading ridges, even though weak hot perturbations might exist beneath small magmatic centers like segment 28 (Figure 4). In that case, such a model with a thick crust and excess melt supply is not exception but a norm at the large magmatic centers along ultraslow spreading ridges, which sequester melts from neighboring cold areas.

Acknowledgments

We thank the Captain and the crew of R/V *Dayang Yihao* for their efforts to complete the first Chinese active-source 3-D OBS experiment in February 2010. We also thank Charles Langmuir and an anonymous reviewer for their thoughtful and insightful comments and suggestions. This work was supported by the MOST grant (2012CB417301), the COMRA grant (DYXM-115-02-3-01), and the NSF China grant (41030857), which supports H. Jian's visit to IPG Paris to complete the 3-D tomography inversion under the supervision of S.C. Singh. The inversion results and data used to generate figures are available upon request via e-mail to the corresponding author.

The Editor thanks Charles Langmuir and an anonymous reviewer for their assistance in evaluating this paper.

References

- Breton, T., F. Nauret, S. Pichat, B. Moine, M. Moreira, E. F. Rose-Koga, D. Auclair, C. Bosq, and L.-M. Wavrant (2013), Geochemical heterogeneities within the Crozet hotspot, *Earth Planet. Sci. Lett.*, *376*, 126–136, doi:10.1016/j.epsl.2013.06.020.
- Canales, J. P., R. S. Detrick, J. Lin, J. A. Collins, and D. R. Toomey (2000), Crustal and upper mantle seismic structure beneath the rift mountains and across a nontransform offset at the Mid-Atlantic Ridge (35°N), *J. Geophys. Res.*, *105*(B2), 2699–2719, doi:10.1029/1999JB900379.
- Cannat, M., C. Rommevaux-Jestin, D. Sauter, C. Deplus, and V. Mendel (1999), Formation of the axial relief at the very slow spreading Southwest Indian Ridge (49° to 69°E), *J. Geophys. Res.*, *104*(B10), 22,825–22,843, doi:10.1029/1999JB900195.
- Cannat, M., C. Rommevaux-Jestin, and H. Fujimoto (2003), Melt supply variations to a magma-poor ultra-slow spreading ridge (Southwest Indian Ridge 61° to 69° E), *Geochem. Geophys. Geosyst.*, *4*(8), 9104, doi:10.1029/2002GC000480.
- Cannat, M., D. Sauter, V. Mendel, E. Ruellan, K. Okino, J. Escartin, V. Combiere, and M. Baala (2006), Modes of seafloor generation at a melt-poor ultraslow-spreading ridge, *Geology*, *34*(7), 605–608, doi:10.1130/g22486.1.
- Cannat, M., M. R. Muller, R. S. White, D. Sauter, A. Bezos, C. Meyzen, E. Humler, and M. Le Rigoleur (2008), Spreading rate, spreading obliquity, and melt supply at the ultraslow spreading Southwest Indian Ridge, *Geochem. Geophys. Geosyst.*, *9*, Q04002, doi:10.1029/2007GC001676.
- Chen, Y. J. (1992), Oceanic crustal thickness versus spreading rate, *Geophys. Res. Lett.*, *19*(8), 753–756, doi:10.1029/92GL00161.
- Dalton, C. A., C. H. Langmuir, and A. Gale (2014), Geophysical and geochemical evidence for deep temperature variations beneath mid-ocean ridges, *Science*, *344*(6179), 80–83, doi:10.1126/science.1249466.
- DeMets, C., R. G. Gordon, D. F. Argus, and S. Stein (1994), Effect of recent revisions to the geomagnetic reversal time scale on estimates of current plate motions, *Geophys. Res. Lett.*, *21*(20), 2191–2194, doi:10.1029/94GL02118.
- Dick, H. J. B., J. Lin, and H. Schouten (2003), An ultraslow-spreading class of ocean ridge, *Nature*, *426*(6965), 405–412, doi:10.1038/nature02128.
- Dunn, R. A., D. R. Toomey, and S. C. Solomon (2000), Three-dimensional seismic structure and physical properties of the crust and shallow mantle beneath the East Pacific Rise at 9°30'N, *J. Geophys. Res.*, *105*(B10), 23,537–23,555, doi:10.1029/2000JB900210.
- Dunn, R. A., V. Lekic, R. S. Detrick, and D. R. Toomey (2005), Three-dimensional seismic structure of the Mid-Atlantic Ridge (35°N): Evidence for focused melt supply and lower crustal dike injection, *J. Geophys. Res.*, *110*, B09101, doi:10.1029/2004JB003473.
- Hoof, E. E. E., R. S. Detrick, D. R. Toomey, J. A. Collins, and J. Lin (2000), Crustal thickness and structure along three contrasting spreading segments of the Mid-Atlantic Ridge, 33.5°–35°N, *J. Geophys. Res.*, *105*(B4), 8205–8226, doi:10.1029/1999JB900442.
- Horner-Johnson, B. C., R. G. Gordon, S. M. Cowles, and D. F. Argus (2005), The angular velocity of Nubia relative to Somalia and the location of the Nubia-Somalia-Antarctica triple junction, *Geophys. J. Int.*, *162*(1), 221–238, doi:10.1111/j.1365-246X.2005.02608.x.
- Jokat, W., and M. C. Schmidt-Aursch (2007), Geophysical characteristics of the ultraslow spreading Gakkel Ridge, Arctic Ocean, *Geophys. J. Int.*, *168*(3), 983–998, doi:10.1111/j.1365-246X.2006.03278.x.
- Jokat, W., J. Kollofrath, W. H. Geissler, and L. Jensen (2012), Crustal thickness and earthquake distribution south of the Logachev Seamount, Knipovich Ridge, *Geophys. Res. Lett.*, *39*, L08302, doi:10.1029/2012GL051199.
- Magde, L. S., and D. W. Sparks (1997), Three-dimensional mantle upwelling, melt generation, and melt migration beneath segment slow spreading ridges, *J. Geophys. Res.*, *102*(B9), 20,571–20,583, doi:10.1029/97JB01278.
- Mahoney, J., A. P. Leroex, Z. Peng, R. L. Fisher, and J. H. Natland (1992), Southwestern limits of Indian Ocean Ridge Mantle and the origin of low ²⁰⁶Pb/²⁰⁴Pb mid-ocean ridge basalt: Isotope systematics of the central Southwest Indian Ridge (17°–50°E), *J. Geophys. Res.*, *97*(B13), 19,771–19,790, doi:10.1029/92JB01424.
- Mendel, V., D. Sauter, C. Rommevaux-Jestin, P. Patriat, F. Lefebvre, and L. M. Parson (2003), Magmato-tectonic cyclicity at the ultra-slow spreading Southwest Indian Ridge: Evidence from variations of axial volcanic ridge morphology and abyssal hills pattern, *Geochem. Geophys. Geosyst.*, *4*(5), 9102, doi:10.1029/2002GC000417.
- Meyzen, C. M., J. N. Ludden, E. Humler, B. Luais, M. J. Toplis, C. Mevel, and M. Storey (2005), New insights into the origin and distribution of the DUPAL isotope anomaly in the Indian Ocean mantle from MORB of the Southwest Indian Ridge, *Geochem. Geophys. Geosyst.*, *6*, Q11K11, doi:10.1029/2005GC000979.
- Michael, P., C. Langmuir, H. Dick, J. Snow, S. Goldstein, D. Graham, K. Lehnert, G. Kurras, W. Jokat, and R. Mühe (2003), Magmatic and amagmatic seafloor generation at the ultraslow-spreading Gakkel ridge, Arctic Ocean, *Nature*, *423*(6943), 956–961, doi:10.1038/nature01704.
- Minshull, T. A., M. R. Muller, and R. S. White (2006), Crustal structure of the Southwest Indian Ridge at 66°E: Seismic constraints, *Geophys. J. Int.*, *166*(1), 135–147, doi:10.1111/j.1365-246X.2006.03001.x.
- Montesi, L. G. J., M. D. Behn, L. B. Hebert, J. Lin, and J. L. Barry (2011), Controls on melt migration and extraction at the ultraslow Southwest Indian Ridge 10°–16°E, *J. Geophys. Res.*, *116*, B10102, doi:10.1029/2011JB008259.
- Puthe, C., and T. Gerya (2014), Dependence of mid-ocean ridge morphology on spreading rate in numerical 3-D models, *Gondwana Res.*, *25*(1), 270–283, doi:10.1016/j.gr.2013.04.005.
- Sauter, D., V. Mendel, C. Rommevaux-Jestin, L. M. Parson, H. Fujimoto, C. Mével, M. Cannat, and K. Tamaki (2004), Focused magmatism versus amagmatic spreading along the ultra-slow spreading Southwest Indian Ridge: Evidence from TOBI side scan sonar imagery, *Geochem. Geophys. Geosyst.*, *5*, Q10K09, doi:10.1029/2004GC000738.
- Sauter, D., M. Cannat, C. Meyzen, A. Bezos, P. Patriat, E. Humler, and E. Debayle (2009), Propagation of a melting anomaly along the ultraslow Southwest Indian Ridge between 46°E and 52°20'E: Interaction with the Crozet hotspot?, *Geophys. J. Int.*, *179*(2), 687–699, doi:10.1111/j.1365-246X.2009.04308.x.
- Sauter, D., M. Cannat, S. Rouméjon, M. Andreani, D. Birot, A. Bronner, D. Brunelli, J. Carlot, A. Delacour, and V. Guyader (2013), Continuous exhumation of mantle-derived rocks at the Southwest Indian Ridge for 11 million years, *Nat. Geosci.*, *6*(4), 314–320, doi:10.1038/ngeo1771.
- Schindwein, V., A. Demuth, W. H. Geissler, and W. Jokat (2013), Seismic gap beneath Logachev Seamount: Indicator for melt focusing at an ultraslow mid-ocean ridge?, *Geophys. Res. Lett.*, *40*, 1703–1707, doi:10.1002/grl.50329.

- Seher, T., W. C. Crawford, S. C. Singh, M. Cannat, V. Comber, and D. Dusanur (2010), Crustal velocity structure of the Lucky Strike segment of the Mid-Atlantic Ridge at 37°N from seismic refraction measurements, *J. Geophys. Res.*, *115*, B03103, doi:10.1029/2009JB006650.
- Shipp, R. M., and S. C. Singh (2002), Two-dimensional full wavefield inversion of wide-aperture marine seismic streamer data, *Geophys. J. Int.*, *151*(2), 325–344, doi:10.1046/j.1365-246X.2002.01645.x.
- Singh, S. C., et al. (2006), Seismic reflection images of the Moho underlying melt sills at the East Pacific Rise, *Nature*, *442*(7100), 287–290, doi:10.1038/nature04939.
- Standish, J. J., H. J. B. Dick, P. J. Michael, W. G. Melson, and T. O'Hearn (2008), MORB generation beneath the ultraslow spreading Southwest Indian Ridge (9–25°E): Major element chemistry and the importance of process versus source, *Geochem. Geophys. Geosyst.*, *9*, Q05004, doi:10.1029/2008GC001959.
- Tao, C. H., et al. (2012), First active hydrothermal vents on an ultraslow-spreading center: Southwest Indian Ridge, *Geology*, *40*(1), 47–50, doi:10.1130/g32389.1.
- Taylor, M. A. J., and S. C. Singh (2002), Composition and microstructure of magma bodies from effective medium theory, *Geophys. J. Int.*, *149*(1), 15–21, doi:10.1046/j.1365-246X.2002.01577.x.
- Tolstoy, M., A. J. Harding, and J. A. Orcutt (1993), Crustal thickness on the Mid-Atlantic Ridge: Bull's-eye gravity anomalies and focused accretion, *Science*, *262*(5134), 726–729, doi:10.1126/science.262.5134.726.
- Van Avendonk, H. J. A., A. J. Harding, J. A. Orcutt, and J. S. McClain (1998), A two-dimensional tomographic study of the Clipperton transform fault, *J. Geophys. Res.*, *103*(B8), 17,885–17,899, doi:10.1029/98JB00904.
- Van Avendonk, H. J. A., D. J. Shillington, W. S. Holbrook, and M. J. Hornbach (2004), Inferring crustal structure in the Aleutian island arc from a sparse wide-angle seismic data set, *Geochem. Geophys. Geosyst.*, *5*, Q08008, doi:10.1029/2003GC000664.
- Zhao, M., et al. (2013), Three-dimensional seismic structure of the Dragon Flag oceanic core complex at the ultraslow spreading Southwest Indian Ridge (49°39'E), *Geochem. Geophys. Geosyst.*, *14*, 4544–4563, doi:10.1002/ggge.20264.
- Zhou, H., and H. J. B. Dick (2013), Thin crust as evidence for depleted mantle supporting the Marion Rise, *Nature*, *494*(7436), 195–200, doi:10.1038/nature11842.